IEEE Access
Multidisciplinary | Rapid Review | Open Access Journal

Received November 19, 2018, accepted December 5, 2018, date of publication December 10, 2018,
date of current version January 4, 2019.

Digital Object Identifier 10.1109/ACCESS.2018.2885988

Control Method for Maximizing Fault Voltage of Wind Generation-Integrated Power Systems With Consideration of DFIG–Grid Coupling

DI ZHENG, (Student Member, IEEE), XIAOFU XIONG, (Member, IEEE), JINXIN OUYANG, (Member, IEEE), ZHEN ZHANG, AND CHAO XIAO

State Key Laboratory of Power Transmission Equipment and System Security and New Technology, School of Electrical Engineering, Chongqing University, Chongqing 400044, China

Corresponding author: Jinxin Ouyang (jinxinoy@163.com)

This work was supported in part by the National Key R&D Program of China under Grant 2016YFB0900600, in part by the National Natural Science Foundation of China under Grant 51877018, and in part by the Technology Projects of State Grid Corporation of China under Grant 52094017000W.

ABSTRACT In the last decade, wind generation techniques have been actively developed, and wind farms comprising doubly-fed induction generators (DFIGs) have been widely deployed. As a result of the increasing penetration of wind generation, the output power of DFIGs requires adjustment to ensure an adequate supply of reactive current under fault conditions. Many studies show that the reactive capability of a DFIG is constrained by the rotor current and terminal voltage. However, the power adjustment of DFIGs changes the grid power flow and the terminal voltage of DFIGs due to the coupling between DFIGs and the grid. The permissible power range of DFIGs also changes because of the terminal voltage variation. The DFIG–grid coupling has not been considered, and the permissible power range is not accurate. The control methods based on the existing permissible power range do not maximize the power controllability of DFIGs. In this paper, the fault power characteristics of DFIGs under the constraints of rotor current and rotor speed are analyzed on the basis of a fault model. The permissible power range of DFIGs with consideration of internal and external constraints is established by analyzing the terminal voltage under the effect of the grid power flow. A control method for maximizing fault voltage is proposed on the basis of the established permissible power range. The simulation results verify the accurate calculation of the permissible power range. The power controllability of DFIGs could be fully utilized to improve fault voltage by adopting the proposed method.

INDEX TERMS Doubly-fed induction generator (DFIG), voltage control, permissible power range, DFIG–grid coupling.

I. INTRODUCTION

With the development of power electric techniques, wind turbines based on doubly-fed induction generators (DFIG) have been widely applied to power systems [1]. Wind turbines are expected to contribute to transient voltage support, frequency regulation, and inertia support, in addition to basic power generation [2]–[4]. Among these ancillary services of wind turbines, fault voltage support has attracted increasing attention from researchers.

The fault voltage needs to be improved to avoid the tripping of wind turbines under the fault and benefit on voltage recovery in the post-fault condition. A supplement of reactive power compensators is an effective solution to realize the fault voltage support of wind farms and improve voltage stability [5]–[7]. However, this solution increases cost and may lead to high voltage and tripping of wind turbines if reactive power compensators are not timely switched off under post-fault conditions [8]. Given the fast and flexible controllability of DFIGs, the use of their own reactive power has been proposed as an alternative. References [9]–[11] devoted efforts to improve the reactive capability of DFIGs through controller structure modification. Additionally, References [12]–[14] discussed the constraints of DFIGs' transient power and focused on optimal reactive power dispatch.

Researchers have been trying to establish a permissible power range to explore the maximum reactive power of

DFIGs [15]–[17]. Reference [15] discussed the factors that influence DFIGs' permissible power range among which MPRC was found to be the most important. In vector-oriented control, the stator power is controlled by the rotor current, which is restricted by the MPRC. Reference [16] specifically addressed the influence of IGBT's junction temperature on the MPRC. Studies on the permissible power range of DFIGs focused on internal constraints and regarded terminal voltage as a static parameter [18]–[21]. However, the influence of grid power flow on DFIGs' terminal voltage has not been considered. Existing voltage control methods usually take the maximum reactive power in the power range as the optimal power reference for transient voltage support [22]–[24]. However, the best fault voltage may not be achieved when the maximum reactive power is provided due to the coupling of active power and reactive power.

The coupling between DFIGs and the grid has strengthened with the increasing application of DFIGs and the deepening exploration of their power controllability. Grid power flow is changed by the transient power of DFIGs and conversely affects the terminal voltage of DFIGs. Hence, the terminal voltage of DFIGs varies with respect to the DFIGs' active and reactive power. The permissible power range also changes with the variation of the terminal voltage. The influence of grid power flow on DFIGs' power range has not been considered in existing studies. The permissible power range in the literature may be not accurate, and existing voltage control methods could not fully utilize the power controllability of DFIGs.

In the present study, the fault power characteristics of DFIGs are analyzed on the basis of a fault model. The constraints of rotor current and rotor speed on the permissible power range are discussed. Then, the permissible power range is established with consideration of internal and external constraints by analyzing the function of DFIGs' terminal voltage under the effect of grid power flow. A control method for maximizing fault voltage is proposed on the basis of the established permissible power range. The simulation results verify the accuracy of the presented permissible power range. The proposed voltage control is proved to be more effective than conventional voltage control methods are in terms of supporting fault voltage.

II. FAULT POWER CHARACTERISTICS OF DFIGS

A. MPRC-CONSTRAINED POWER CHARACTERISTICS

The rotating turbine of a DFIG provides mechanical power while the rotor-side converter (RSC) provides excitation. Owing to the wide frequency range of RSCs, DFIGs are able to operate in a wide wind speed range. The voltage and flux linkage equations of DFIG in the synchronous reference frame are as follows:

$$\begin{cases} \boldsymbol{u}_s = R_s \boldsymbol{i}_s + j\omega_s \boldsymbol{\psi}_s + d\boldsymbol{\psi}_s/dt \\ \boldsymbol{u}_r = R_r \boldsymbol{i}_r + js\omega_s \boldsymbol{\psi}_r + d\boldsymbol{\psi}_r/dt \\ \boldsymbol{\psi}_s = L_s \boldsymbol{i}_s + L_m \boldsymbol{i}_r \\ \boldsymbol{\psi}_r = L_r \boldsymbol{i}_r + L_m \boldsymbol{i}_s \end{cases} \tag{1}$$

where $\boldsymbol{u}_s$ and $\boldsymbol{u}_r$ are the stator and rotor voltage vectors, respectively; $\boldsymbol{i}_s$ and $\boldsymbol{i}_r$ are the stator and rotor current vectors, respectively; $\boldsymbol{\psi}_s$ and $\boldsymbol{\psi}_r$ are the stator and rotor flux linkage vectors; R_s and R_r are the stator- and rotor-side resistances, respectively; L_s and L_r are the stator- and rotor-side inductances, respectively; L_m is the excitation inductance; ω_s is the synchronous speed and s is the slip ratio.

When the grid fault occurs, the stator voltage dip results in transient components in the stator and rotor electrical quantities, especially the flux linkages. To avoid devices damage by high transient components, a general solution is to activate the crowbar and shut down the RSC [25]. A reasonable crowbar resistance contributes to fast decaying of transient components and recovery of the DFIG control. The RSC will be restarted and the crowbar will be removed when the rotor current recovers to normal level. In the RSC control period, the fundamental frequency components are the main of currents and flux linkages [26]. Therefore, the equation of stator voltage in (1) can be transformed as

$$\boldsymbol{u}_{sf} = R_s \boldsymbol{i}_{sf} + j\omega_s \boldsymbol{\psi}_{sf} \tag{2}$$

where the subscript 'f' represents electrical quantities under the grid fault.

By substituting the stator flux linkage equation in (1) into (2), the stator voltage is obtained as [27]

$$\boldsymbol{u}_{sf} = (R_s + jX_s)\,\boldsymbol{i}_{sf} + jX_m \boldsymbol{i}_{rf} \tag{3}$$

where $X_s = j\omega_s L_s$ and $X_r = j\omega_s L_r$ are the stator-side and equivalent rotor-side reactances, respectively; $X_m = j\omega_s L_m$ is the excitation reactance.

Based on the instantaneous power theory, the stator current can be expressed as

$$\boldsymbol{i}_{sf} = \frac{-P_{sf} + jQ_{sf}}{\hat{\boldsymbol{u}}_{sf}} \tag{4}$$

where P_{sf} and Q_{sf} are the active and reactive power of the stator, respectively. The superscript '^' represents the conjugation of the stator voltage vector.

By substituting (4) into (3), the rotor current can be obtained as

$$\boldsymbol{i}_{rf} = \frac{\boldsymbol{u}_{sf}}{jX_m} - \frac{R_s + jX_s}{jX_m}\frac{-P_{sf} + jQ_{sf}}{\hat{\boldsymbol{u}}_{sf}} \tag{5}$$

Equation (5) indicates that the stator power is controlled by the rotor current. The amplitude of the rotor current is written as

$$I_{rf}^2 = \frac{\left(P_{sf}X_s - Q_{sf}R_s\right)^2 + \left(U_{sf}^2 + P_{sf}R_s + Q_{sf}X_s\right)^2}{X_m^2 U_{sf}^2} \tag{6}$$

where U_{sf} is the amplitude of the terminal voltage.

The rotor current should not exceed the MPRC I_{rmax} to avoid damaging the RSC. Derived from (6), the following equation is obtained as

$$\left(P_{sf} - Y_{rc1}U_{sf}^2\right)^2 + \left(Q_{sf} - Y_{rc2}U_{sf}^2\right)^2 \le I_{rc}^2 U_{sf}^2 \tag{7}$$

where $Y_{rc1} = -R_s/Z_s^2, Y_{rc2} = -X_s/Z_s^2, I_{rc} = X_m I_{rmax}/Z_s$, and $Z_s^2 = R_s^2 + X_s^2$.

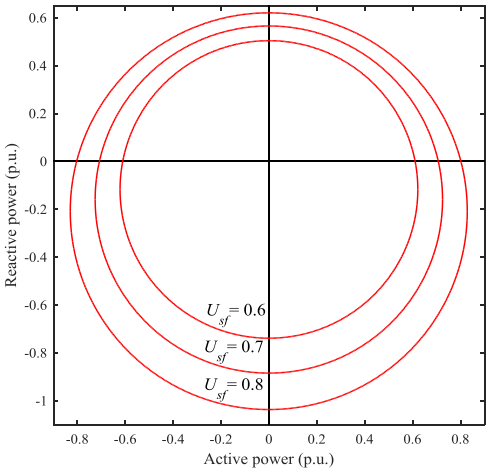

FIGURE 1. MPRC-constrained power range of DFIG.

When only the internal constraint is considered, the terminal voltage is a constant. Thus, (7) is a circle with the center of point $(Y_{\rm rc1}U_{sf}^2, Y_{\rm rc2}U_{sf}^2)$ and radius of $I_{rc}U_{sf}$ in the coordinate plane of $P_{sf} - Q_{sf}$ (Fig. 1). The operation points of a DFIG on the circle indicate the active and reactive power required to achieve a certain terminal voltage. The operation points within the circle region indicate the permissible power range under the constraints of the MPRC and a certain terminal voltage, that is, the internal constrained power range (ICPR). The radius of the circle increases, and the center point moves far from the horizontal axis as the terminal voltage increases. Y_{rc1} is small because of the small stator resistance. Hence, the horizontal position of the center of the circle changes slightly when the terminal voltage increases.

The DFIG operates at unity power factor before the grid fault. After the grid fault, the output power of the DFIG should be adjusted to satisfy the grid code. With the coupling between the DFIG and the grid, the power adjustment of the DFIG changes the grid power flow and furtherly its own terminal voltage. The terminal voltage of the DFIG varies with respect to its active and reactive power instead of being a constant. The circle region represented by (7) could not accurately denote the permissible power range under the influence of grid power flow.

B. ROTOR SPEED-CONSTRAINED POWER CHARACTERISTICS

A DFIG is driven by the mechanical power supplied by a turbine. In a normal operation, the mechanical power and electromagnetic power are balanced. As grid fault occurs, the electromagnetic power drops, and the power balance is interrupted, leading to rotor acceleration. The rotor motion equation can be expressed as

$$\int \left(P_m - P_{sf}\right) dt = M\left(\omega_r - \omega_{r0}\right) \tag{8}$$

where M is the rotor inertia, ω_{r0} is the initial rotor speed before the fault, and P_m is the mechanical power.

The emergency pitch control is activated immediately after the grid fault occurs to avoid over speeding and DFIG tripping. The average pitch regulation speed is usually 10°/s. By utilizing the numerical fitting method, the mechanical power can be obtained as [28]

$$P_m = P_w C_p = P_w\left(-0.0173t^2 - 0.1467t + 0.4382\right) \tag{9}$$

where P_w is the power absorbed from the wind and C_p is the power coefficient.

The rotor speed does not reach the maximum value until the mechanical power P_m decreases to P_{sf}. As a result of the unpredictable duration of the fault, the maximum rotor speed should be kept lower than the permissible value. By combining (8) and (9), the rotor speed of the DFIG under grid fault is expressed as

$$\omega_r = \omega_{r0} - \frac{P_w}{M}t\left(0.0058t^2 - 0.0734t + 0.4382 - P_{sf}/P_w\right) \tag{10}$$

On the basis of the derivation of (10), the maximum rotor speed can be given by

$$\omega_{r\,\max} = \omega_{r0} - 4.2163\frac{0.6444P_w - P_{sf}}{M} + 5.0530\frac{0.7510P_w - P_{sf}}{M}\sqrt{0.7409 - \frac{P_{sf}}{P_w}} \tag{11}$$

The minimum permissible active power of the DFIG $P_{sf.ao}$ is obtained as

$$P_{sf.ao} = P_w\eta \tag{12}$$

where η is the minimum real root of the following equation:

$$\eta^3 - 1.5466\eta^2 + (0.7795 - 0.3303\varepsilon)\,\eta + 0.03917\varepsilon^2 + 0.2128\varepsilon - 0.1288 = 0$$

in which $\varepsilon = M(\omega_{rpa} - \omega_{r0})/P_w$ and ω_{rpa} is the maximum permissible rotor speed.

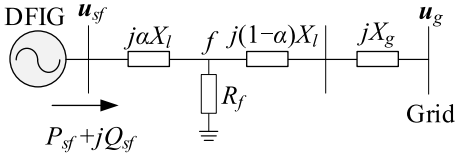

FIGURE 2. DFIG-integrated power system.

III. PERMISSIBLE POWER RANGE OF DFIG WITH CONSIDERATION OF EXTERNAL CONSTRAINT

A. BOUNDARY OF PERMISSIBLE POWER RANGE

The DFIG-integrated power system is shown in Fig. 2. The DFIG connects to an equivalent grid through a transmission line with the reactance of X_l. The voltage of the equivalent grid is $\boldsymbol{u}_g$, and the equivalent reactance is X_g. The three-phase

fault occurs at the point on the transmission line that is α times the whole line length away from the DFIG. The fault resistance is R_f. The circuit equation of the system is

$$\frac{\left(R_f + jX'_g\right)\boldsymbol{u}_{sf} - R_f\boldsymbol{u}_g}{-X'_dX'_g + jR_f\left(X'_g + X'_d\right)} = \frac{P_{sf} - jQ_{sf}}{\hat{\boldsymbol{u}}_{sf}} \tag{13}$$

where $X'_g = (1-\alpha)X_l + X_g + X_{Tg}$, $X'_d = \alpha X_l + X_{Td}$. X_{Tg} is the reactance of the transformer between the transmission line and the equivalent grid. X_{Td} is the reactance of the DFIG's step-up transformer.

By solving (13), the terminal voltage equation is obtained as

$$\left(P_{sf} - Y_{pf1}U_{sf}^2\right)^2 + \left(Q_{sf} - Y_{pf2}U_{sf}^2\right)^2 = I_{pf}^2U_{sf}^2 \tag{14}$$

where

$$\begin{aligned}
Y_{pf1} &= -\frac{R_fX'^2_g}{X_{d1}^2X'^2_g + R_f^2\left(X_{d1}+X'_g\right)^2}\\
Y_{pf2} &= -\frac{X_{d1}X'^2_g + R_f^2\left(X_{d1}+X'_g\right)}{X_{d1}^2X'^2_g + R_f^2\left(X_{d1}+X'_g\right)^2}\\
I_{pf} &= \frac{R_fU_g}{\sqrt{X_{d1}^2X'^2_g + R_f^2\left(X_{d1}+X'_g\right)^2}}
\end{aligned}$$

Equation (14) indicates the effect of grid power flow on the terminal voltage of the DFIG, which varies with respect to the active and reactive power of the DFIG. Therefore, the permissible power region changes with the variation of the operation points. By substituting (14) into (7), the equation of the permissible power range is obtained as

$$AP_{sf}^2 + BP_{sf}Q_{sf} + CQ_{sf}^2 + DP_{sf} + EQ_{sf} + F \le 0 \tag{15}$$

where

$$\begin{aligned}
A &= \left[\left(Y_{rc1}^2 + Y_{rc2}^2\right) - \left(Y_{pf1}^2 + Y_{pf2}^2\right)\right]^2\\
&\quad + 4\left(Y_{rc1} - Y_{pf1}\right)\left[Y_{rc1}\left(Y_{pf1}^2 + Y_{pf2}^2\right) - Y_{pf1}\left(Y_{rc1}^2 + Y_{rc2}^2\right)\right]\\
B &= 4\left\{\left(Y_{rc1} - Y_{pf1}\right)\left[Y_{rc2}\left(Y_{pf1}^2 + Y_{pf2}^2\right) - Y_{pf2}\left(Y_{rc1}^2 + Y_{rc2}^2\right)\right]\right.\\
&\quad \left. + \left(Y_{rc2} - Y_{pf2}\right)\left[Y_{rc1}\left(Y_{pf1}^2 + Y_{pf2}^2\right) - Y_{pf1}\left(Y_{rc1}^2 + Y_{rc2}^2\right)\right]\right\}\\
C &= \left[\left(Y_{rc1}^2 + Y_{rc2}^2\right) - \left(Y_{pf1}^2 + Y_{pf2}^2\right)\right]^2\\
&\quad + 4\left(Y_{rc2} - Y_{pf2}\right)\left[Y_{rc2}\left(Y_{pf1}^2 + Y_{pf2}^2\right) - Y_{pf2}\left(Y_{rc1}^2 + Y_{rc2}^2\right)\right]\\
D &= 2\left\{\left(Y_{pf1}^2 + Y_{pf2}^2\right)\left[\left(2Y_{rc1} - Y_{pf1}\right)I_{rc}^2 - Y_{rc1}I_{pf}^2\right]\right.\\
&\quad \left. + \left(Y_{rc1}^2 + Y_{rc2}^2\right)\left[\left(2Y_{pf1} - Y_{rc1}\right)I_{pf}^2 - Y_{pf1}I_{rc}^2\right]\right\}\\
E &= 2\left\{\left(Y_{pf1}^2 + Y_{pf2}^2\right)\left[\left(2Y_{rc2} - Y_{pf2}\right)I_{rc}^2 - Y_{rc2}I_{pf}^2\right]\right.\\
&\quad \left. + \left(Y_{rc1}^2 + Y_{rc2}^2\right)\left[\left(2Y_{pf2} - Y_{rc2}\right)I_{pf}^2 - Y_{pf2}I_{rc}^2\right]\right\}\\
F &= \left(I_{rc}^2 - I_{pf}^2\right)\left[\left(Y_{pf1}^2 + Y_{pf2}^2\right)I_{rc}^2 - \left(Y_{rc1}^2 + Y_{rc2}^2\right)I_{pf}^2\right]
\end{aligned}$$

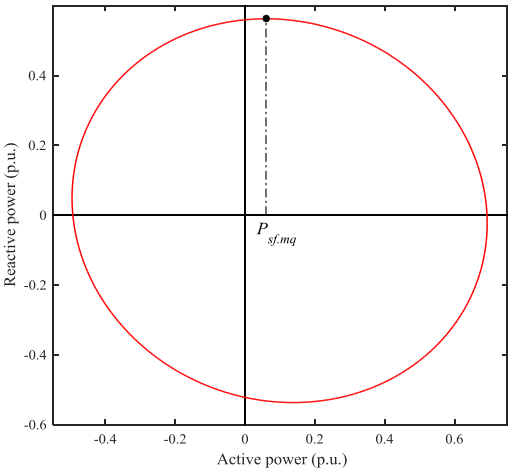

FIGURE 3. Internal and external constrained power range of DFIG.

A is not equal to C, and therefore, (15) indicates an ellipse in the coordinate plane of $P_{sf} - Q_{sf}$ (Fig. 3). The region in the ellipse represents the permissible power range of the DFIG under the constraints of the rotor current and grid power flow, that is, the internal and external constrained power range (IECPR). As U_{sf} is absent in (15), the IECPR is only related to the parameters of the DFIG and the grid and not to the operational conditions. The IECPR benefits the power dispatch and control strategy design.

B. MAXIMUM REACTIVE POWER IN PERMISSIBLE POWER RANGE

According to (15), the operation points of the DFIG on the boundary of the ellipse can be expressed as

$$CQ_{sf}^2 + \left(BP_{sf} + E\right)Q_{sf} + AP_{sf}^2 + DP_{sf} + F = 0 \tag{16}$$

As the DFIG is generally used to supply reactive power, the large root of (16) can be solved as

$$Q_{sp} = \frac{\sqrt{\left(BP_{sf}+E\right)^2 - 4C\left(AP_{sf}^2 + DP_{sf} + F\right)} - \left(BP_{sf}+E\right)}{2C} \tag{17}$$

By deriving Q_{sp} with respect to P_{sf}, P_{sf}, which makes Q_{sp} achieve the maximum value, can be obtained as

$$P_{sf.mq} = \frac{BE-2CD}{4AC-B^2} - \sqrt{\left(\frac{BE-2CD}{4AC-B^2}\right)^2 - \frac{CD^2+B^2F-BDE}{A\left(4AC-B^2\right)}} \tag{18}$$

Equation (18) indicates that Q_{sp} increases as P_{sf} increases when $P_{sf} < P_{sf.mq}$; otherwise, Q_{sp} decreases as P_{sf} increases. Additionally, if $P_{sf.mq}$ is lower than the minimum permissible active power $P_{sf.ao}$, Q_{sp} achieves the maximum value when $P_{sf} = P_{sf.ao}$. Thus, the maximum reactive power

in the permissible power range is

$$Q_{sf.\max}=\begin{cases}\dfrac{\sqrt{\left(BP_{sf.mq}+E\right)^2-4C\left(AP_{sf.mq}^2+DP_{sf.mq}+F\right)}}{2C}\\ -\dfrac{\left(BP_{sf.mq}+E\right)}{2C},\ P_{sf.mq}>P_{sf.ao}\\ \dfrac{\sqrt{\left(BP_{sf.ao}+E\right)^2-4C\left(AP_{sf.ao}^2+DP_{sf.ao}+F\right)}}{2C}\\ -\dfrac{\left(BP_{sf.ao}+E\right)}{2C},\ P_{sf.mq}\le P_{sf.ao}\end{cases}\tag{19}$$

IV. CONTROL METHOD FOR MAXIMIZING FAULT VOLTAGE BASED ON PERMISSIBLE POWER RANGE

A. CONTROL PURPOSE AND REFERENCES

The ICPR and IECPR are compared in Fig. 4. The solid red ellipse represents the boundary of the IECPR while the dashed black circle indicates the boundary of the ICPR. The circle with point o_k at the center and radius of $I_{rc}U_{sk}$ intersects at points k_1 and k_2 with the ellipse. The circle with point o_m at the center and radius of $I_{rc}U_{sm}$ is tangent to the ellipse at point m. After the effect of grid power flow is considered, the shape and area of the permissible power range change, which reflects the variation of power controllability.

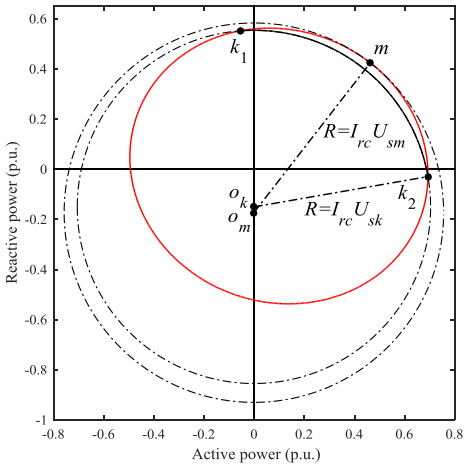

FIGURE 4. Comparison between IECPR and ICPR.

The dashed black circle denotes a set of the required operation points for a certain terminal voltage. Given the significance of the ellipse, the part of the circle within the ellipse region indicates the available operation points for a certain terminal voltage. For example, the solid segment k_1k_2 on circle o_k indicates that the terminal voltage can achieve U_{sk} when the DFIG operates at the segment k_1k_2. The same is not true for the part beyond the ellipse. With regard to circle o_m, only one point (point m) is noted on the circle within the ellipse that makes the terminal voltage achieve U_{sm}. Point m denotes the maximum terminal voltage that the DFIG is able to achieve in the permissible power range.

By substituting (17) into (14), the terminal voltage when the DFIG operates at the points on the ellipse is obtained as

$$U_{sf}^2=\frac{\left[B\left(Y_{rc2}-Y_{pf2}\right)-2C\left(Y_{rc1}-Y_{pf1}\right)\right]}{CG}P_{sf}+\frac{E\left(Y_{rc2}-Y_{pf2}\right)+C\left(I_{pf}^2-I_{rc}^2\right)-\left(Y_{rc2}-Y_{pf2}\right)\sqrt{\Delta}}{CG}\tag{20}$$

where

$$\Delta=\left(B^2-4AC\right)P_{sf}^2+(2BE-4CD)P_{sf}+\left(E^2-4CF\right)$$
$$G=\left(Y_{pf1}^2+Y_{pf2}^2\right)-\left(Y_{rc1}^2+Y_{rc2}^2\right).$$

The derivation of (20) with respect to P_{sf} is given by

$$\frac{dU_{sf}^2}{dP_{sf}}=\frac{B\left(Y_{rc2}-Y_{pf2}\right)-2C\left(Y_{rc1}-Y_{pf1}\right)}{CG}-\frac{\left(Y_{rc2}-Y_{pf2}\right)\left[\left(B^2-4AC\right)P_{sf}+(BE-2CD)\right]}{\sqrt{\Delta}}\tag{21}$$

Equation (21) equals zero, that is, U_{sf} achieves the maximum value when $P_{sf}=P_{sf.mv}$:

$$P_{sf.mv}=\frac{BE-2CD}{4AC-B^2}-\left[1+\frac{E^2-4CF}{4AC-B^2}-\frac{AE^2+CD^2-BDE-4ACF+B^2F}{\left(4AC-B^2\right)(1+H)G^2}\right]^{1/2}\tag{22}$$

where

$$H=\left(Y_{rc1}-Y_{pf1}\right)^2/\left(Y_{rc2}-Y_{pf2}\right)^2$$

For the operation points on the ellipse, the terminal voltage increases as P_{sf} increases when $P_{sf}<P_{sf.mv}$; otherwise, the terminal voltage decreases as P_{sf} increases.

If $P_{sf.mv}>P_{sf.ao}$, the DFIG does not overspeed when delivering the active power of $P_{sf.mv}$. By substituting $P_{sf.mv}$ into (17)The corresponding reactive power $Q_{sf.mv}$ can be solved as

$$Q_{sf.mv}=\frac{\sqrt{\left(BP_{sf.mv}+E\right)^2-4C\left(AP_{sf.mv}^2+DP_{sf.mv}+F\right)}}{2C}-\frac{BP_{sf.mv}+E}{2C}\tag{23}$$

Therefore, the maximum terminal voltage in the permissible power range is obtained as

$$U_{sf.\max}=\left\{\frac{\left[B\left(Y_{rc2}-Y_{pf2}\right)-2C\left(Y_{rc1}-Y_{pf1}\right)\right]}{CG}P_{sf.mv}+\frac{E\left(Y_{rc2}-Y_{pf2}\right)+C\left(I_{pf}^2-I_{rc}^2\right)}{CG}-\frac{\sqrt{\left(BP_{sf.mv}+E\right)^2-4C\left(AP_{sf.mv}^2+DP_{sf.mv}+F\right)}}{CG}\right\}^{1/2}\tag{24}$$

If $P_{sf.mv} \le P_{sf.ao}$, then the DFIG overspeeds when delivering the active power of $P_{sf.mv}$. For this condition, the terminal voltage reach the maximum value with the active power of $P_{sf.ao}$ under the premise of safety. The corresponding reactive power and maximum terminal voltage are as follows:

$$Q_{sf.ao} = -\frac{BP_{sf.ao}+E}{2C} + \frac{\sqrt{\left(BP_{sf.ao}+E\right)^2-4C\left(AP_{sf.ao}^2+DP_{sf.ao}+F\right)}}{2C} \tag{25}$$

$$U_{sf.\max} = \left\{\frac{\left[B\left(Y_{rc2}-Y_{pf2}\right)-2C\left(Y_{rc1}-Y_{pf1}\right)\right]}{C\left[\left(Y_{pf1}^2+Y_{pf2}^2\right)-\left(Y_{rc1}^2+Y_{rc2}^2\right)\right]}P_{sf.ao} + \frac{E\left(Y_{rc2}-Y_{pf2}\right)+C\left(I_{pf}^2-I_{rc}^2\right)}{CG} - \frac{\sqrt{\left(BP_{sf.ao}+E\right)^2-4C\left(AP_{sf.ao}^2+DP_{sf.ao}+F\right)}}{CG}\right\}^{1/2} \tag{26}$$

B. FLOW CHART OF PROPOSED METHOD

In maximizing the terminal voltage of the DFIG under the fault, the fault power of the DFIG should be dispatched according to the calculation results under different conditions. The flow chart of control method for maximizing fault voltage is illustrated in Fig. 5. First, the fault position α and fault resistance R_f are calculated as followings:

$$\alpha = \frac{\lambda_1 U_{sf0}^2}{\left(\lambda_1 Q_{sf0}+\lambda_2 P_{sf0}\right)X_l} - \frac{X_{Td}}{X_l} \tag{27}$$

$$R_f = \frac{\lambda_1 P_{sf0} U_{sf0}^4}{\left(\lambda_1 Q_{sf0}+\lambda_2 P_{sf0}\right)^2} - \frac{\left(X_g'+X_d'\right)P_{sf0}U_{sf0}^2}{\lambda_1 Q_{sf0}+\lambda_2 P_{sf0}} \tag{28}$$

where

$$\lambda_1 = U_{sf0}^2 - U_g U_{sf0}\cos\theta_{df0} + \left(X_g'+X_d'\right)Q_{sf0}$$

$$\lambda_2 = U_g U_{sf0}\sin\theta_{df0} + \left(X_g'+X_d'\right)P_{sf0}$$

where U_{sf0} and θ_{sf0} are the measured amplitude and phase angle of DFIG's terminal voltage following the fault; P_{sf0} and Q_{sf0} are the measured active and reactive power of DFIG following the fault.

Then the boundary of the IECPR is calculated by (15). $P_{sf.ao}$ and $P_{sf.mv}$ are calculated by (12) and (22), respectively. The corresponding reactive power $Q_{sf.mv}$ and $Q_{sf.ao}$ with respect to $P_{sf.mv}$ and $P_{sf.ao}$ can be calculated by (23) and (25), respectively. If $P_{sf.mv} > P_{sf.ao}$, then the power references $P_{sf.ref}$ and $Q_{sf.ref}$ are set to $P_{sf.mv}$ and $Q_{sf.mv}$, respectively; otherwise, $P_{sf.ref}$ and $Q_{sf.ref}$ are set to $P_{sf.ao}$ and $Q_{sf.ao}$, respectively. Finally, the proposed control is activated, and the power references of the outer loop of the RSC are switched to $P_{sf.ref}$ and $Q_{sf.ref}$ when the grid fault occurs.

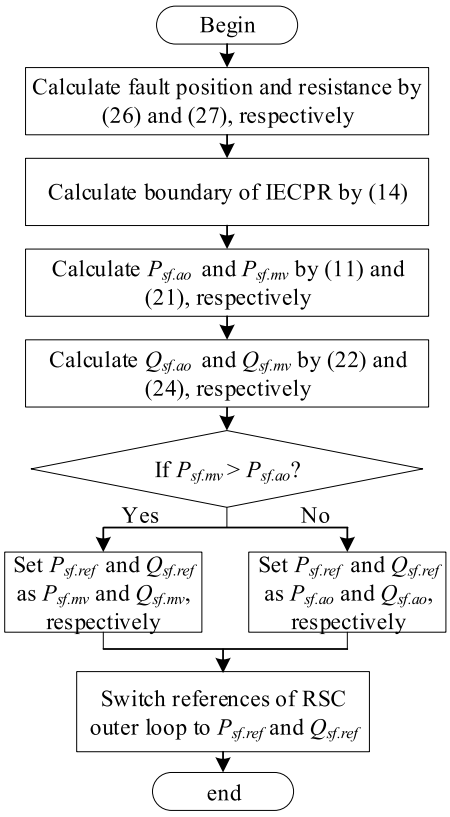

FIGURE 5. Flow chart of proposed method.

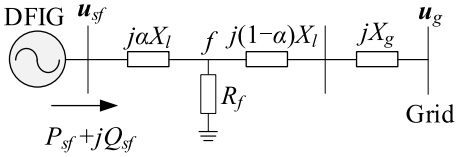

FIGURE 6. Structure of simulation system.

V. CASE STUDY

A. VERIFICATION OF PERMISSIBLE POWER RANGE

The simulation system shown in Fig. 6 is built in MATLAB/Simulink. The DFIG connects to the equivalent 110 kV grid through a 50 km transmission line. The short-circuit capacity of the equivalent grid is 10 MVA. The detailed parameters of the DFIG are listed in the Appendix. The DFIG operates in the normal rated condition with the rotor speed of 1.2 p.u. before the fault. The maximum permissible rotor speed is 1.3 p.u.. The wind speed is 15 m/s. A three-phase fault occurs at the middle of the transmission line when $t = 0.5$ s. The proposed voltage control is activated immediately following the fault, and the grid-side converter (GSC) continues to operate at

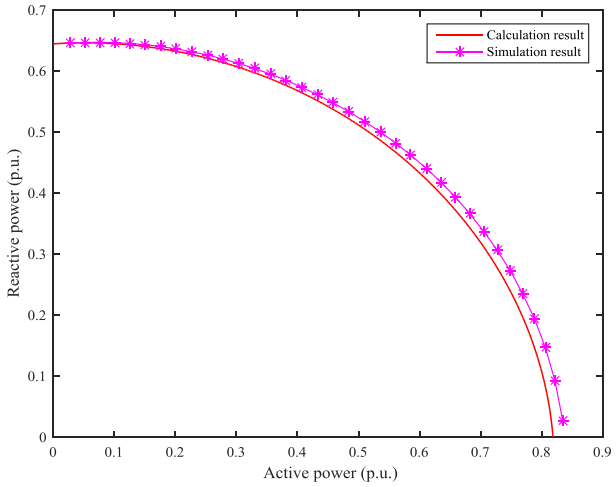

(a)

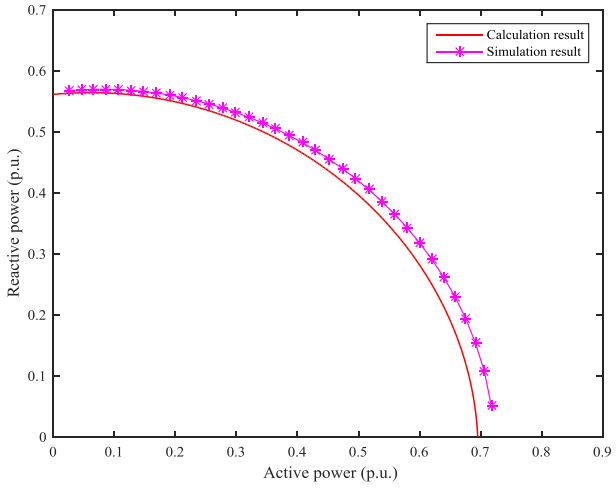

(b)

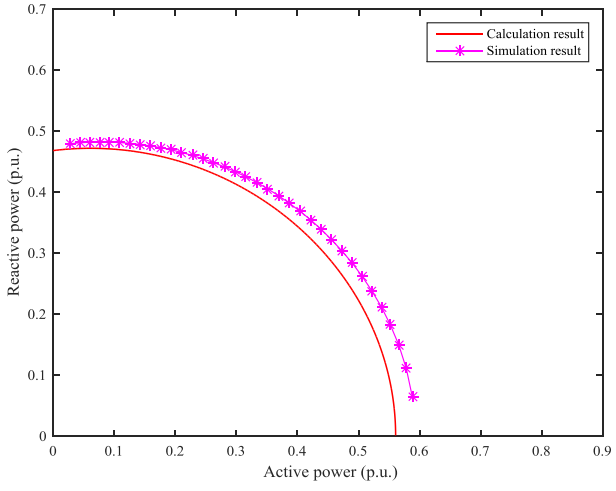

(c)

FIGURE 7. IECPR of the DFIG when fault resistances are (a) 100 Ω, (b) 70 Ω, and (c) 50 Ω.

unity power factor. $P_{sf.ao}$ is calculated as 0.1033 p.u. by (12). The boundaries of the IECPR calculated by (15) under the fault resistances of 100, 70, and 50 Ω are compared with simulation results in Fig. 7.

The comparison indicates that the calculation results agree with the simulation result and that the theoretical analysis is accurate. The permissible power range indeed changes from a circle into an ellipse when the coupling between the DFIG and the grid is considered. The errors between the theoretical and simulation results are caused by the disregard for the active power transferred by the GSC. However, the active power of the GSC is low under the grid fault, and the resulting errors are relatively small.

B. VERIFICATION OF PROPOSED VOLTAGE CONTROL METHOD

Two methods are compared to verify the effectiveness of the proposed method. The proposed method is regarded as Case 1. In Case 2, the DFIG supplies reactive current according to the grid code given by

$$i_Q = 1.5\left(0.9 - U_{pcc}\right)$$

where U_{pcc} is the voltage amplitude of the point of common coupling (PCC).

In Case 3, the DFIG has the same reactive power as Case 1, and the active power retains its minimum value of $P_{sf.ao}$.

1) Scenario 1

The fault resistance is set to 100 Ω, and the PCC voltage falls to 0.70 p.u. following the fault. $P_{sf.ref}$ and $Q_{sf.ref}$ calculated by the proposed method in Case 1 are 0.4790 and 0.5252 p.u., respectively. The theoretical maximum voltage of the PCC in the IECPR is calculated as 0.8789 p.u. The reactive current in Case 2 should be 0.30 p.u. Accordingly, the active and reactive power references in Case 2 should be 0.6261 and 0.21 p.u., respectively. The active and reactive power references in Case 3 are 0.1033 and 0.5252 p.u., respectively. The DFIG active and reactive power, rotor current and the PCC voltage amplitude are shown in Fig. 8.

The PCC voltage amplitudes in the three cases are 0.8960, 0.8580, and 0.8395 p.u., respectively. The voltage amplitude of the PCC in Case 1 improves by 4.43% and 6.73% relative to the values in Case 2 and Case 3, respectively.

2) Scenario 2

The fault resistance is set to 70 Ω, and the PCC voltage falls to 0.58 p.u. following the fault. $P_{sf.ref}$ and $Q_{sf.ref}$ calculated by the proposed method in Case 1 are 0.4650 and 0.4258 p.u., respectively. The theoretical maximum voltage of the PCC in the IECPR is calculated as 0.7309 p.u. The reactive current in Case 2 should be 0.48 p.u. Accordingly, the active and reactive power references in Case 2 should be 0.4692 and 0.2784 p.u., respectively. The active and reactive power references in Case 3 are 0.1033 and 0.4258 p.u., respectively. The DFIG active and reactive power, rotor current and the PCC voltage amplitude are shown in Fig. 9.

The PCC voltage amplitudes in the three cases are 0.7560, 0.7324, and 0.6943 p.u., respectively. The voltage amplitude of the PCC in Case 1 improves by 3.22% and 8.89% relative to the values in Case 2 and Case 3, respectively.

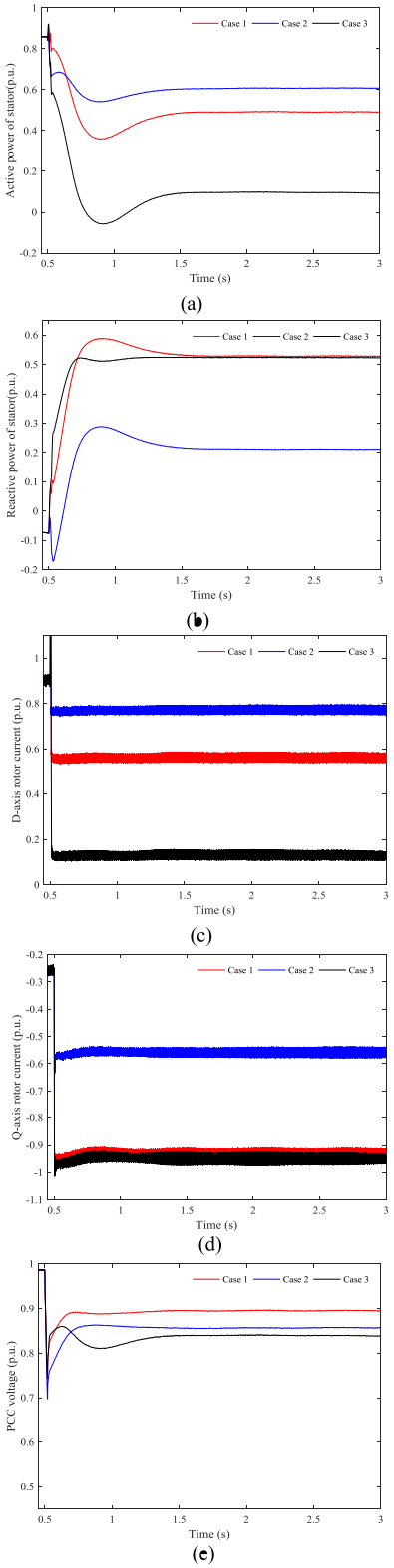

FIGURE 8. Simulation results in Scenario 1 (a) active power, (b) reactive power, (c) d-axis rotor current, (d) q-axis rotor current and (e) PCC voltage.

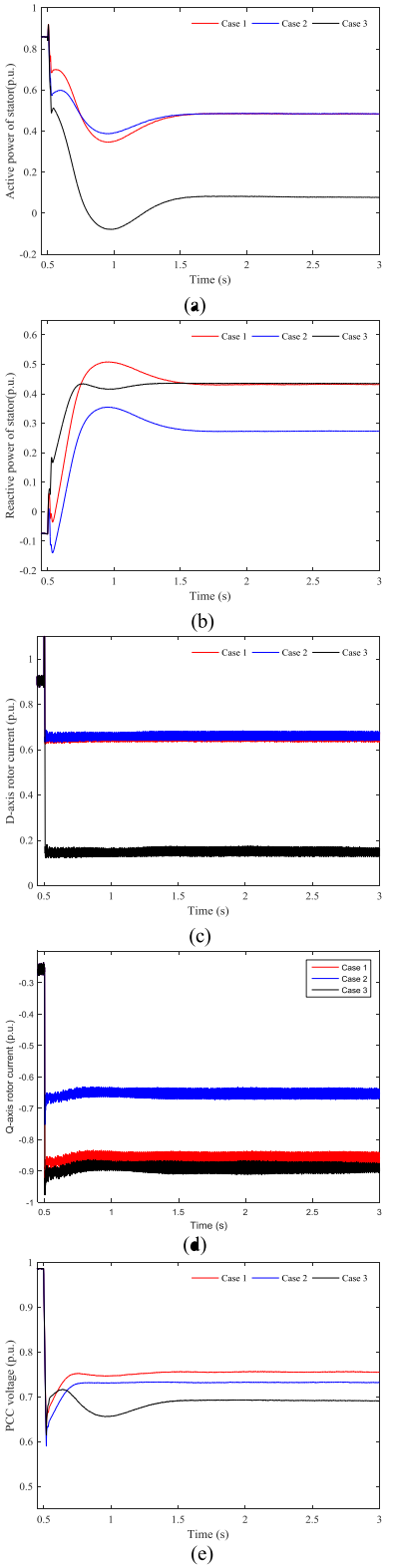

FIGURE 9. Simulation results in Scenario 2 (a) active power, (b) reactive power, (c) d-axis rotor current, (d) q-axis rotor current and (e) PCC voltage.

3) Scenario 3

The fault resistance is set to 50 Ω, and the PCC voltage falls to 0.48 p.u. following the fault. $P_{sf.ref}$ and $Q_{sf.ref}$ calculated by the proposed method in Case 1 are 0.4014 and 0.3426 p.u., respectively. The theoretical maximum voltage of the PCC in the IECPR is calculated as 0.5832 p.u. The reactive current

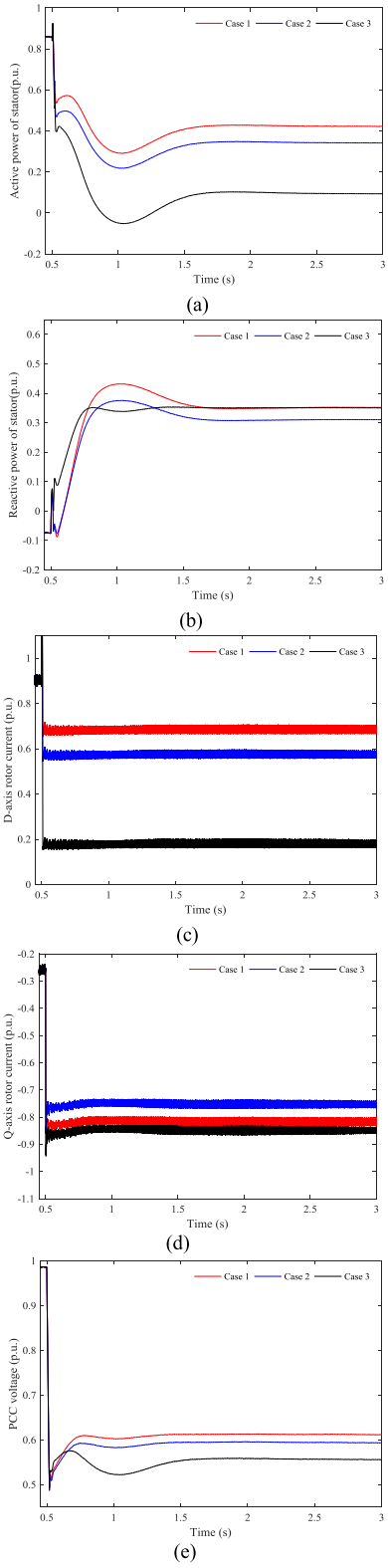

FIGURE 10. Simulation results in Scenario 3. (a) active power, (b) reactive power, (c) d-axis rotor current, (d) q-axis rotor current and (e) PCC voltage.

in Case 2 should be 0.63 p.u. Accordingly, the active and reactive power references in Case 2 should be 0.3257 and 0.3024 p.u., respectively. The active and reactive power

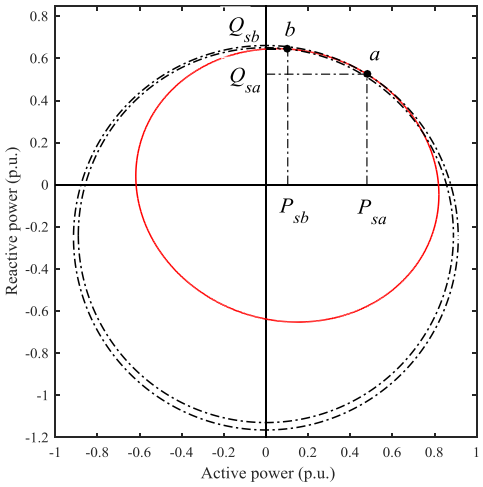

FIGURE 11. Comparison of maximum voltage control and maximum reactive power control.

references in Case 3 are 0.1033 and 0.3426 p.u., respectively. The DFIG active and reactive power, rotor current and the PCC voltage amplitude are shown in Fig. 10.

The PCC voltage amplitudes in the three cases are 0.6105, 0.5911, and 0.5560 p.u., respectively. The voltage amplitude of the PCC in Case 1 improves by 3.28% and 9.80% relative to the values in Case 2 and Case 3, respectively.

The simulation results indicate that the proposed method can improve the PCC voltage under different fault resistance conditions and that it is more effective than the other two methods are.

4) Scenario 4

In this scenario, the PCC voltage improvements of the proposed method and the maximum reactive power control are compared. The fault resistance is set to 100 Ω, and the IECPR of the DFIG is shown in Fig. 11. Point *a* is the operating point that makes the terminal voltage reach the maximum. The active and reactive power of Point *a* are 0.4790 and 0.5252 p.u., respectively. The theoretical maximum PCC voltage in the IECPR is calculated as 0.8789 p.u. Point *b* is the operating point that has the maximum reactive power. The active and reactive power of Point *b* are 0.1033 and 0.6449 p.u., respectively because $P_{sf.ao} > P_{sf.mq}$. The theoretical PCC voltage when the DFIG operates at Point *b* is calculated as 0.8569 p.u.

The electrical quantities of Points *a* and *b* are illustrated in Fig. 12. The practical active and reactive power of the DFIG agree with the theoretical results. The practical PCC voltages of Points *a* and *b* are 0.8858 and 0.8602 p.u., respectively. The PCC voltage of Point *a* is improved by 2.98% relative to the PCC voltage of Point *b*. Meanwhile, the active power of Point *b* is only 21.57% of that of Point *a*. The maximum reactive power control sacrifices the active power for reactive power support, which may result in the lack of active power in the power system and instability. The proposed method maintains a large active power

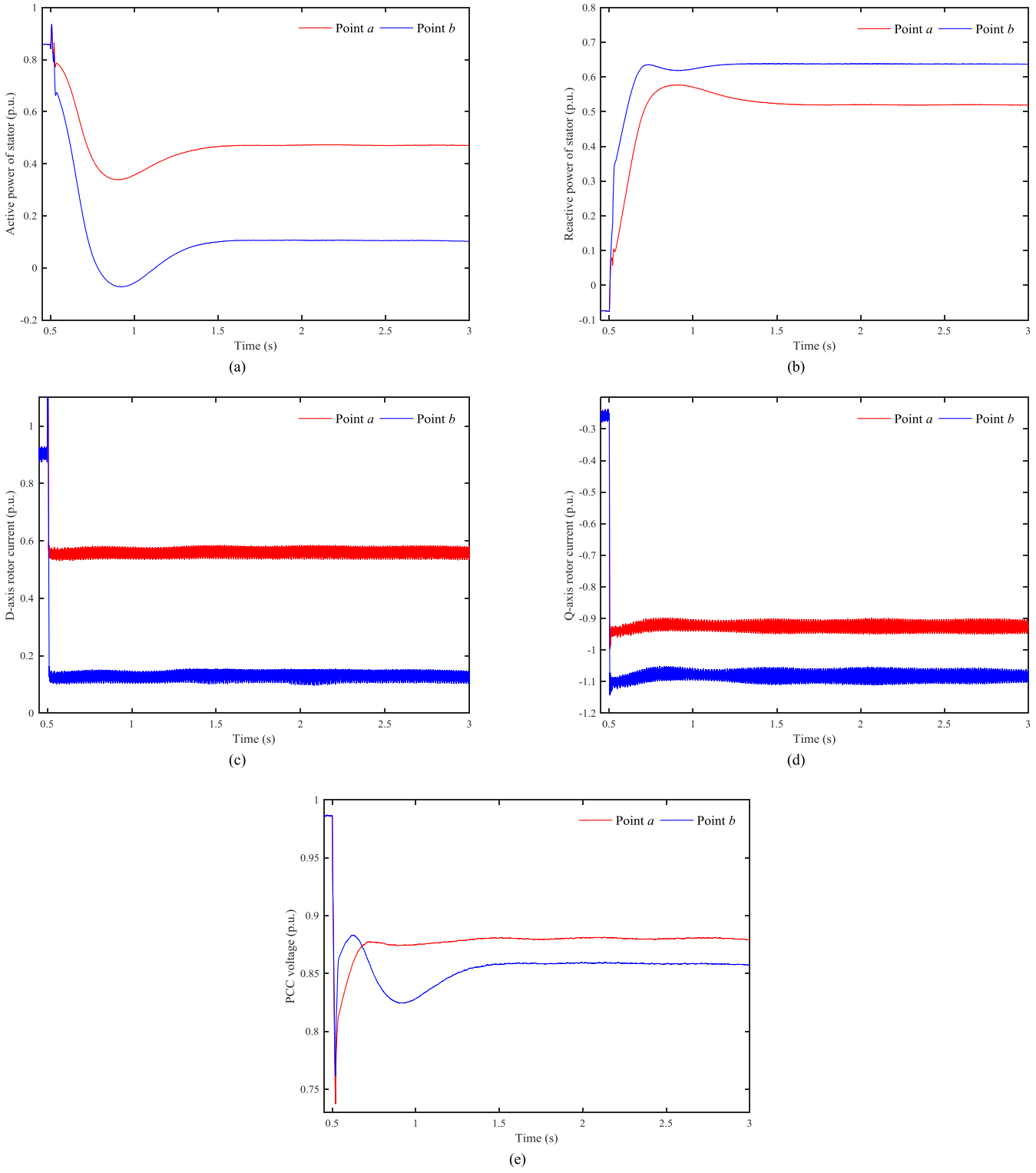

FIGURE 12. Simulation results when proposed method and maximum reactive power control adopted respectively (a) active power of DFIG, (b) reactive power of DFIG, (c) d-axis rotor current of DFIG, (d) q-axis rotor current, and (e) PCC voltage.

when supporting the fault voltage. Active power shortage and instability are avoided when the proposed method is adopted.

VI. CONCLUSIONS

The coupling between DFIGs and the grid has not been considered in existing studies on permissible power range.

The permissible power range in the literature may not be accurate, and the controllability of DFIGs has not been fully utilized to support the fault voltage. In the present study, the fault power characteristics of a DFIG under the constraints of rotor current and rotor speed are analyzed on the basis of a fault model. The permissible power range under the constraints of rotor current and grid power flow is established by analyzing the influence of grid power flow on the terminal voltage of the DFIG. Different from existing conclusions, the shape and area of the permissible power range undergo drastic changes when the coupling between the DFIG and the grid is considered. The control method for maximizing fault voltage is proposed on the basis of the established permissible power range with consideration of internal and external constraints. The simulation results demonstrate that the proposed method can improve the fault voltage and active power output. The use of the proposed method benefits the safety and stability of the power system better than maximum reactive power control methods could.

APPENDIX

The parameters of DFIG simulation model are as follows:

Rated voltage: 575 V.
Rated capacity: 1.5 MW.
Rated frequency: 60 Hz.
Stator resistance: 0.0071 p.u.
Rotor resistance: 0.005 p.u.
Stator leakage inductance: 0.1714 p.u.
Rotor leakage inductance: 0.1563 p.u.
Magnetizing inductance: 2.9 p.u.

REFERENCES

[1] D. Zheng, A. T. Eseye, J. Zhang, and H. Li, "Short-term wind power forecasting using a double-stage hierarchical ANFIS approach for energy management in microgrids," *Protection Control Mod. Power Syst.*, vol. 2, no. 2, p. 13, Apr. 2017.
[2] M. Edrah, K. L. Lo, and O. Anaya-Lara, "Reactive power control of DFIG wind turbines for power oscillation damping under a wide range of operating conditions," *IET Generat. Transmiss. Distrib*, vol. 10, no. 15, pp. 3777–3785, Nov. 2016.
[3] D. Yang, J. Kim, Y. C. Kang, E. Muljadi, N. Zhang, and J. Hong, "Temporary frequency support of a DFIG for high wind power penetration," *IEEE Trans. Power Syst.*, vol. 33, no. 3, pp. 3428–3437, May 2018.
[4] J. Kim, J.-K. Seok, E. Muljadi, and Y. C. Kang, "Adaptive $Q-V$ scheme for the voltage control of a DFIG-based wind power plant," *IEEE Trans. Power Electron.*, vol. 31, no. 5, pp. 3586–3599, May 2015.
[5] W. Qiao, R. G. Harley, and G. K. Venayagamoorthy, "Coordinated reactive power control of a large wind farm and a STATCOM using heuristic dynamic programming," *IEEE Trans. Energy Convers.*, vol. 24, no. 2, pp. 493–503, Jun. 2009.
[6] R. Ou, X.-Y. Xiao, Z.-C. Zou, Y. Zhang, and Y.-H. Wang, "Cooperative control of SFCL and reactive power for improving the transient voltage stability of grid-connected wind farm with DFIGs," *IEEE Trans. Appl. Supercond.*, vol. 26, no. 7, Oct. 2016, Art. no. 5402606.
[7] Q. Lv, Z. Xu, H. Li, J. Xiao, and S. Wang, "Effects of dynamic reactive power compensation on wind farm transient voltage and its control strategy research," *Electr. Power Construction*, vol. 36, no. 8, pp. 122–129, Aug. 2015.
[8] Y. Wang, Q. Wu, H. Xu, Q. Guo, and H. Sun, "Fast coordinated control of DFIG wind turbine generators for low and high voltage ride-through," *Energies*, vol. 7, no. 7, pp. 4140–4156, Jul. 2014.
[9] M. Mohseni and S. M. Islam, "Transient control of DFIG-based wind power plants in compliance with the Australian grid code," *IEEE Trans. Power Electron.*, vol. 27, no. 6, pp. 2813–2824, Jun. 2012.
[10] G. Tapia, A. Tapia, and J. X. Ostolaza, "Proportional–integral regulator-based approach to wind farm reactive power management for secondary voltage control," *IEEE Trans. Energy Convers.*, vol. 22, no. 2, pp. 488–498, Jun. 2007.
[11] D. Xie, Z. Xu, L. Yang, J. Østergaard, Y. Xue, and K. P. Wong, "A comprehensive LVRT control strategy for DFIG wind turbines with enhanced reactive power support," *IEEE Trans. Power Syst.*, vol. 28, no. 3, pp. 3302–3310, Aug. 2013.
[12] J. Martínez, P. C. Kjær, P. Rodriguez, and R. Teodorescu, "Design and analysis of a slope voltage control for a DFIG wind power plant," *IEEE Trans. Energy Convers.*, vol. 27, no. 1, pp. 11–20, Mar. 2012.
[13] J. Kim, E. Muljadi, J.-W. Park, and Y. C. Kang, "Adaptive hierarchical voltage control of a DFIG-based wind power plant for a grid fault," *IEEE Trans. Smart Grid*, vol. 7, no. 6, pp. 2980–2990, Nov. 2016.
[14] S. Mondal and D. Kastha, "Maximum active and reactive power capability of a matrix converter-fed DFIG-based wind energy conversion system," *IEEE J. Emerg. Sel. Topics Power Electron.*, vol. 5, no. 3, pp. 1322–1333, Sep. 2017.
[15] S. Engelhardt, I. Erlich, J. Kretschmann, F. Shewarega, and C. Feltes, "Reactive power capability of wind turbines based on doubly fed induction generators," *IEEE Trans. Energy Convers.*, vol. 26, no. 1, pp. 364–372, Mar. 2011.
[16] M. Z. Sujod, I. Erlich, and S. Engelhardt, "Improving the reactive power capability of the DFIG-based wind turbine during operation around the synchronous speed," *IEEE Trans. Energy Convers.*, vol. 28, no. 3, pp. 736–745, Sep. 2013.
[17] R. J. Konopinski, P. Vijayan, and V. Ajjarapu, "Extended reactive capability of DFIG wind parks for enhanced system performance," *IEEE Trans. Power Syst.*, vol. 24, no. 3, pp. 1346–1355, Aug. 2009.
[18] J. Ouyang, T. Tang, Y. Diao, M. Li, and J. Yao, "Control method of doubly fed wind turbine for wind speed variation based on dynamic constraints of reactive power," *IET Renew. Power Generat.*, vol. 12, no. 9, pp. 973–980, Jul. 2018.
[19] T. Lund, P. Sørensen, and J. Eek, "Reactive power capability of a wind turbine with doubly fed induction generator," *Wind Energy*, vol. 10, no. 4, pp. 379–394, Jul. 2007.
[20] Q. Liu and Z. Wang, "Reactive power generation mechanism & characteristic of doubly fed variable speed constant frequency wind power generator," *Proc. CSEE*, vol. 31, no. 3, pp. 82–89, Jan. 2011.
[21] D. Santos-Martin, S. Arnaltes, and A. J. L. Rodriguez, "Reactive power capability of doubly fed asynchronous generators," *Electr. Power Syst. Res.*, vol. 78, no. 11, pp. 1837–1840, Nov. 2008.
[22] B. Kanna and S. N. Singh, "Towards reactive power dispatch within a wind farm using hybrid PSO," *Int. J. Elect. Power Energy Syst.*, vol. 69, pp. 232–240, Jul. 2015.
[23] Y. Li, Z. Xu, J. Zhang, and K. Meng, "Variable droop voltage control for wind farm," *IEEE Trans. Sustain. Energy*, vol. 9, no. 1, pp. 491–493, Jan. 2018.
[24] B. Zhang, W. Hu, P. Hou, J. Tan, M. Soltani, and Z. Chen, "Review of reactive power dispatch strategies for loss minimization in a DFIG-based wind farm," *Energies*, vol. 10, no. 7, p. 856, Jul. 2017.
[25] R. Cardenas, R. Pena, S. Alepuz, and G. Asher, "Overview of control systems for the operation of DFIGs in wind energy applications," *IEEE Trans. Ind. Electron.*, vol. 60, no. 7, pp. 2776–2798, Jul. 2013.
[26] X. Kong, Z. Zhang, X. Yin, and M. Wen, "Study of fault current characteristics of the DFIG considering dynamic response of the RSC," *IEEE Trans. Energy Convers.*, vol. 29, no. 2, pp. 278–287, Jun. 2014.
[27] S. Boubzizi, H. Abid, A. El Hajjaji, and M. Chaabane, "Comparative study of three types of controllers for DFIG in wind energy conversion system," *Protection Control Mod. Power Syst.*, vol. 3, no. 1, p. 21, Sep. 2018.
[28] D. Zheng, J. Ouyang, X. Xiong, C. Xiao, and M. Li, "A system transient stability enhancement control method using doubly fed induction generator wind turbine with considering its power constraints," *Energies*, vol. 11, no. 4, p. 945, Apr. 2018.

DI ZHENG (S'18) received the B.E. degree in electrical engineering from Chongqing University, Chongqing, China, in 2014, where he is currently pursuing the Ph.D. degree with the School of Electrical Engineering. His current research interests include the control and protection of wind power-integrated power system.

XIAOFU XIONG (M'05) received the B.E., M.E., and Ph.D. degrees in electrical engineering from Chongqing University, Chongqing, China, in 1982, 1986, and 2005, respectively. He is currently a Professor with the School of Electrical Engineering, Chongqing University. His current research interests include smart grid, power system control, and protection.

JINXIN OUYANG (M'15) received the B.E. and Ph.D. degrees in electrical engineering from Chongqing University, Chongqing, China, in 2012, respectively. He is currently a Professor with the School of Electrical Engineering, Chongqing University. His current research interests include analysis, protection, and control of renewable energy integrated power system.

ZHEN ZHANG received the B.E. degree in electrical engineering from Chongqing University, Chongqing, China, in 2018, where she is currently pursuing the M.E. degree with the School of Electrical Engineering. Her current research interests include protection and control of renewable energy integrated power system.

CHAO XIAO received the B.E. degree in automation from the Zhongyuan University of Technology, Zhengzhou, China, in 2006, and the M.E. degree in control engineering from Chongqing University, Chongqing, China, in 2010, where he is currently pursuing the Ph.D. degree in electrical engineering. His current research interests include power system control and protection.